Inorganic Chemistry

ARTICLE

pubs.acs.org/IC

Stability and Structural Evolution of $Ce^{IV}_{1-x}Ln^{III}_xO_{2-x/2}$ Solid Solutions: A Coupled μ-Raman/XRD Approach

D. Horlait,[†] L. Claparède,[†,‡] N. Clavier,[†] S. Szenknect,[†] N. Dacheux,*[,†] J. Ravaux,[†] and R. Podor[†]

[†]ICSM-UMR5257 CNRS/CEA/UM2/ENCSM, Site de Marcoule, Bât. 426, BP 17171, 30207 Bagnols/Cèze, France

[‡]CEA/DEN/DRCP/SCPS/LC2A, Site de Marcoule, BP 17171, 30207 Bagnols/Cèze Cedex, France

Supporting Information

ABSTRACT: Several CeO_2-based mixed oxides with general composition $Ce_{1-x}Ln_xO_{2-x/2}$ (for $0 \le x \le 1$ and Ln = La, Nd, Sm, Eu, Gd, Dy, Er, or Yb) were prepared using an initial oxalic precipitation leading to a homogeneous distribution of cations in the oxides. After characterization of the Ce/Nd oxalate precursors and then thermal conversion to oxides at $T = 1000$ °C, investigation of the crystalline structure of these oxides was carried out by XRD and μ-Raman spectroscopy. Typical fluorite $Fm\bar{3}m$ structure was obtained for relatively low Ln^{III} contents, while a cubic $Ia\bar{3}$ superstructure was evidenced above $x \approx 0.4$. Moreover, since Nd_2O_3 does not crystallize with the $Ia\bar{3}$-type structure, two-phase systems composed with additional hexagonal Nd_2O_3 were obtained for $x_{Nd} \ge 0.73$ in the $Ce_{1-x}Nd_xO_{2-x/2}$ series. The effect of heat treatment temperature on these limits was explored through μ-Raman spectroscopy, which allowed determining the presence of small amounts of the different crystal structures observed. In addition, the variation of the $Ce_{1-x}Ln_xO_{2-x/2}$ unit cell parameter was found to follow a quadratic relation as a result of the combination between increasing cationic radius, modifications of cation coordination, and decreasing O−O repulsion caused by oxygen vacancies.

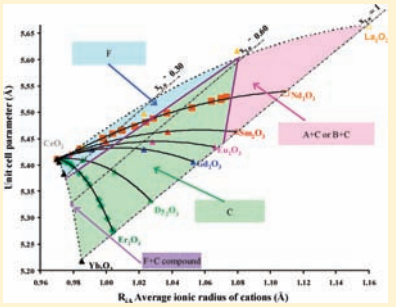

1. INTRODUCTION

During recent years, ceria-based mixed oxides with general composition $Ce_{1-x}Ln_xO_{2-x/2}$ have been considerably studied, mainly as a potential solid electrolyte for intermediate-temperature solid oxide fuel cells (IT-SOFCs), since such materials exhibit great ionic conductivity and are thermodynamically stable at IT-SOFCs working temperature.[1−5]

Moreover, these ceramics are often proposed to foresee the behavior of nuclear fuels since ceria is commonly used to simulate actinides dioxides, particularly plutonium dioxide.[6] Indeed, $Ce^{IV}O_2$ crystallizes in the same structure as $Pu^{IV}O_2$ and $U^{IV}O_2$ (fluorite, $Fm\bar{3}m$ space group: JCPDS files 01-081-0792,[7] 00-051-0798,[8] and 01-073-2293,[9] for CeO_2, PuO_2 and UO_2, respectively), and Ce^{4+} ion presents a close ionic radius compared to plutonium whatever the coordination considered.[10] Similarly, lanthanide oxides ($Ln^{III}_2O_3$) are usually envisaged as nonradioactive analogues for actinide sesquioxides ($An^{III}_2O_3$) such as Am_2O_3 and Cm_2O_3. In these conditions, $Ce_{1-x}Ln_xO_{2-x/2}$ oxides can stand as model compounds for advanced nuclear fuels considered, for instance, in the framework of the development of the fourth generation of nuclear reactors.[11−13] Indeed, several concepts like sodium-cooled fast reactor (SFR) or gas-cooled fast reactor (GFR) plan to operate the recycling of minor actinides, including neptunium, americium, and curium, within fuels such as $(U,Pu)O_2$ mixed oxide (MOx) or inside UO_2-based blankets surrounding the core.[11,14] The effect of the incorporation of trivalent cations in the fluorite-type AnO_2 oxides on several properties of interest such as the sintering capability and the chemical durability is not clearly established. Investigation of the crystal structure of Ln^{III}-doped ceria was first undertaken as a preliminary study, before future works on $Th_{1-x}Ln_xO_{2-x/2}$ and $U_{1-x}Ln_xO_{2-x/2}$ models.

Several papers have been already dedicated to the structural investigation of ceria-based mixed oxides.[15] In particular, it is well known that CeO_2 crystallizes in the fluorite structure (noted F). Incorporation of a trivalent lanthanide in CeO_2 is then obtained through direct substitution of Ce^{4+} by Ln^{3+} along with formation of one-half an oxygen vacancy to counterbalance the lack of positive charges[16−19] as follows

$$Ln_2O_3 + 2Ce^{\times}_{Ce} + O^{\times}_{O} \xrightarrow{CeO_2} 2Ln'_{Ce} + 2CeO_2 + V^{\bullet\bullet}_{O} \quad (1)$$

Formation of a cubic superstructure ($Ia\bar{3}$ space group, thereby noted C) is generally observed for $x \ge 0.4$ (depending on the nature of the doping rare-earth element)[18−29] [JCPDS file 00-028-0267], except for La doping.[30,31] This structure is maintained up to $x = 1$ for lanthanides ranging from europium to lutetium, the C-type structure being stabilized for the sesquioxides based on these cations.[32−34] For lighter lanthanides (such as La, Nd, and Sm), Ln_2O_3 does not commonly crystallize in the C structure and a secondary phase is then formed for high x_{Ln} values. Indeed, as La_2O_3[30,31] and Nd_2O_3 are often reported with the hexagonal structure (space group $P\bar{3}1m$, noted A in the following sections, [JCPDS file 00-043-1023]),[32,35] incorporation limits in CeO_2 are reported for $x_{La} \approx 0.5$[30,36] and for $x_{Nd} \approx 0.7$.[18−22] Besides, since Sm_2O_3 is often obtained in the

Received: April 12, 2011
Published: June 29, 2011

monoclinic form depending on the synthesis conditions[32,35] [JCPDS file 00-043-1030], a secondary phase was reported for $x_{Sm} \geq 0.9$ in $Ce_{1-x}Sm_xO_{2-x/2}$.[18,24]

Nevertheless, it appears that such solubility limits of Ln^{III} in CeO_2 F- and C-type structures differ strongly depending on the studies. In particular, some data tend to confirm that they are influenced by the chemical route of synthesis and/or the conditions of heat treatment. For instance, while Malecka et al.[28] obtained single-phase $Ce_{1-x}Lu_xO_{2-x/2}$ solid solutions for the whole composition range after heating at 950 °C under O_2 atmosphere, they observed formation of two phases, i.e., with F- and C-type structures, when heating the samples containing 40−70% of lutetium up to 1100 °C. This phase separation was also stated by Shuk et al.[23] for $Ce_{1-x}Eu_xO_{2-x/2}$ samples prepared through hydrothermal conditions (T = 260 °C, autogenous pressure). Conversely, Mandal et al.[24] obtained single-phase samples after heating to 1400 °C whatever the europium amount initially considered by using a solid state route from mixtures of Eu_2O_3 and CeO_2. Several other examples concerning $Ce_{1-x}Gd_xO_{2-x/2}$,[25,37] $Ce_{1-x}La_xO_{2-x/2}$,[38] and $Ce_{1-x}Sm_xO_{2-x/2}$[22,24] solid solutions were also mentioned and pointed out that formation of F- and C-type solid solutions seems to strongly depend on these two key parameters: the synthesis route and the heat treatment conditions.

Moreover, even if several data sets are available in the literature for various $Ce_{1-x}Ln_xO_{2-x/2}$ systems, no systematic study has been undertaken in the whole REE series to investigate the effect of incorporation of trivalent lanthanides in CeO_2 structure, especially in terms of unit cell deformation. In this context, this paper presents a study of the effect of the temperature of heat treatment on the two structures stability limits existing for $Ce_{1-x}Nd_xO_{2-x/2}$ solid solutions prepared from oxalate coprecipitates. The quantitative and homogeneous precipitation of lanthanide elements with oxalic acid was chosen to prepare precursors of expected solid solutions since such precursors are usually linked to an improvement of the final sample homogeneity[39−44] and to optimization of some properties of interest, such as sintering capability or chemical durability.[43−48]

After preliminary investigation of Ce/Nd mixed oxalate precursors and their conversion to oxide, this paper describes structural and microstructural characterization of Ce/Ln^{III} mixed oxides with the general formula $Ce_{1-x}Ln^{III}{}_xO_{2-x/2}$ (Ln = La, Nd, Sm, Eu, Gd, Dy, Er, or Yb). In particular, the study concerning $Ce_{1-x}Nd_xO_{2-x/2}$ and $Ce_{1-x}Er_xO_{2-x/2}$ compounds was emphasized in order to compare the systems incorporating light and heavy rare-earth elements.

Finally, X-ray powder diffraction (XRD) and μ-Raman spectroscopy were employed as complementary techniques to underline the effect of heat treatment on the solubility limits of neodymium in F- and C-type structures, on the one hand, and to explore the effects of Ln^{3+} incorporation on the crystal structure obtained, on the other. Furthermore, the variation of the unit cell parameters versus the Ln^{III} substitution ratio in $Ce_{1-x}Ln_xO_{2-x/2}$ solid solutions was examined.

2. EXPERIMENTAL SECTION

Synthesis. $CeCl_3 \cdot 7H_2O$ and $LnCl_3 \cdot nH_2O$ (Aldrich, ≥ 99.9% chemical purity) were used as starting reagents for synthesizing mixed-oxide samples. They were dissolved with the desired stoichiometry in 0.5 M HNO_3 solution to obtain final concentrations of about 0.1 M in cations. The mixture was then quickly poured into a large excess of 0.45 M oxalic acid (Merck, ≥99% purity) at room temperature under stirring, leading to instantaneous precipitation of oxalates solid solutions as follows

$$(1-x)Ce^{3+} + xLn^{3+} + \frac{3}{2}H_2C_2O_4 + yH_2O \xrightarrow{0.5M\ HNO_3} Ce_{1-x}Ln_x(C_2O_4)_{1.5} \cdot yH_2O + 3H^+ \quad (2)$$

The oxalate precipitates were then filtered, washed several times with deionized water, and dried at 90 °C. Their characterization by means of μ-Raman spectroscopy confirmed formation of oxalate-based metal organic frameworks[40,49,50] through observation of characteristic C−C and C−O related vibration modes, while XRD patterns systematically revealed single-phase compounds fitting well with the $P2_1/c$ space group of the $Ln(C_2O_4)_{1.5} \cdot 5H_2O$ lanthanide oxalates [JCPDS file 00-020-0268].[51] The μ-Raman spectrum and XRD pattern of $Ce_{0.715}Nd_{0.285}(C_2O_4)_{1.5} \cdot 5H_2O$ are given in the Supporting Information as examples.

Furthermore, the lanthanides elementary concentrations were determined in the supernatant for all samples by means of ICP-AES analyses (performed on a Spectro Arcos EOP). Whatever the sample considered, less than 1% of the total amount of lanthanide elements remained in solution, showing that lanthanide oxalate precipitation was quantitative (precipitation yield higher than 99%), as expected from the low solubilities reported in the literature for trivalent lanthanide oxalates.[52]

Oxalate samples turned into oxides by heating at 1000 °C in air for 1 h in alumina boats, as described in eq 3. Under these oxidizing conditions, Ce^{III} was spontaneously oxidized into Ce^{IV}.

$$Ce^{III}_{1-x}Ln^{III}_x(C_2O_4)_{1.5} \cdot yH_2O \xrightarrow{1000°C,\ 1h} Ce^{IV}_{1-x}Ln^{III}_xO_{2-x/2} + (2-x/2)CO\uparrow + (1+x/2)CO_2\uparrow + yH_2O\uparrow \quad (3)$$

TG/TD Analysis. Thermal conversion of Ce/Nd mixed oxalates to the corresponding mixed oxides was followed using TG/TD (thermogravimetric/thermodifferential) analyses performed on a Setsys Evolution model (Setaram). The furnace was operating from room temperature to 1000 °C with a heating rate of 5 °C·min^{-1} in order to reproduce the conditions employed for oxalate conversion.

XRD Measurements. X-ray powder diffraction (XRD) patterns were collected between 15° and 80° ($\theta-2\theta$ mode) using a Bruker D8 Advance X-ray diffractometer (Cu K$\alpha_{1,2}$ radiation, λ = 1.5418 Å) equipped with a linear Lynx-eye detector. The XRD pattern of corundum (NIST standard reference material 676a) was used as a reference to estimate the resolution of the apparatus. A step of 0.01° (2θ) and a counting time of 1.5 s·step^{-1} were routinely considered and increased to 0.005° and 6.4 s·step^{-1} for accurate peak analysis. Moreover, as lanthanum oxide is known to be hygroscopic,[53] $Ce_{1-x}La_xO_{2-x/2}$ solid solutions were dried several hours at 90 °C and then transferred into an anoxic and anhydrous glovebox to be sealed in hemispheric airtight sample holders before XRD measurements.

The lattice parameters were refined from powder diffraction profiles using a profile matching procedure implemented in the Fullprof suite software.[54]

Average ionic radii (R_{iA}) reported in Table 1 were calculated such as

$$R_{iA} = (1-x_{Ln})R_{i(Ce)} + x_{Ln}R_{i(Ln)} \quad (4)$$

where x_{Ln} is the mole ratio of the considered lanthanide element and $R_{i(Ce)}$ and $R_{i(Ln)}$ are the ionic radius of Ce^{4+} and Ln^{3+} ions in 8-fold coordination.[10]

μ-Raman. μ-Raman spectra were collected with a Horiba-Jobin Yvon Aramis apparatus equipped with an edge filter and using a He−Ne (λ = 633 nm) laser. The laser beam was focused on the sample using an Olympus BX 41 microscope, resulting in a spot area of about 1 μm^2. At least two different locations were investigated at the surface of each

dx.doi.org/10.1021/ic200751m |Inorg. Chem. 2011, 50, 7150–7161

Table 1. Experimental (EDS) and Expected Mixed-Oxide Compositions with Corresponding Unit Cell Parameters (a), Crystalline Structures, and Average Ionic Radii of Cations (R_{iA})

loading element	expected x ($Ce_{1-x}Ln_xO_{2-x/2}$)	experimental x (EDS)	R_{iA} (Å)	phase type	F or C unit cell parameters (Å) [a]
CeO_2	0.000	0	0.970	F	5.41134 (8)
La	0.100	0.085	0.986	F	5.43464 (5)
	0.300	0.280	1.023	F	5.49759 (10)
	0.600	0.580	1.080	F	5.61684 (14)
Nd	0.100	0.100	0.984	F	5.43022 (8)
	0.200	0.200	0.998	F	5.45084 (11)
	0.250	0.240	1.004	F	5.45943 (13)
	0.300	0.285	1.010	F	5.46671 (9)
	0.350	0.340	1.017	F	5.47365 (10)
	0.400	0.390	1.024	F [b]	5.4814 (2)
	0.450	0.420	1.028	C	5.4884 (2)
	0.500	0.480	1.037	C	5.49910 (13)
	0.600	0.590	1.052	C	5.5066 (2)
	0.700	0.675	1.064	C	5.5214 (2)
	0.730	0.720	1.070	C	5.5268 (2)
	0.750	0.730	1.071	C + A	5.5291 (2)
	0.800	0.765	1.076	C + A	5.5311 (2)
	0.900	0.900	1.093	C + A	5.5312 (3)
	0.980	0.965	1.104	C + A + B	
	1.000	1.000	1.109	A	
Sm	0.100	0.075	0.978	F	5.42153 (9)
	0.300	0.275	1.000	F	5.44415 (9)
	0.600	0.620	1.037	C	5.46245 (14)
	1.000	1.000	1.079	A	
Eu	0.100	0.075	0.977	F	5.41816 (6)
	0.300	0.285	0.997	F	5.4356 (9)
	0.600	0.605	1.028	C	5.44395(14)
Gd	0.100	0.075	0.976	F	5.41679 (8)
	0.300	0.260	0.991	F	5.42908 (10)
	0.600	0.635	1.023	C	5.42905 (14)
Dy	0.100	0.105	0.976	F	5.41180 (9)
	0.300	0.275	0.986	F	5.40936 (8)
	0.600	0.615	1.005	C	5.38747 (14)
Er	0.100	0.100	0.973	F	5.4081 (2)
	0.150	0.145	0.975	F	5.40650 (9)
	0.200	0.195	0.977	F	5.4052 (3)
	0.250	0.245	0.978	F	5.4019 (4)
	0.300	0.285	0.980	F	5.39705 (11)
	0.400	0.390	0.983	C	5.38539 (9)
	0.450	0.405	0.984	C	5.38545 (15)
	0.500	0.505	0.987	C	5.37380 (10)
	0.600	0.585	0.990	C	5.3624 (2)
	0.750	0.745	0.995	C	5.3342 (2)
	0.800	0.795	0.997	C	5.32243 (7)
	0.900	0.900	1.001	C	5.2985 (3)
	1.000	1.000	1.004	C	5.27622 (7)
Yb	0.100	0.080	0.971	F	5.40528 (9)
	0.300	0.285	0.974	F	5.38309 (9)
	0.600	0.600	0.979	F + C	5.3376 (2)

[a] For comparison purpose, only a and $a/2$ were reported for F- and C-type structures, respectively. Standard uncertainties are given with refinement results by Fullprof. [b] C phase was detected by μ-Raman.

sample, usually considering a dwell time of 3 s and an average of 10 scans. μ-Raman bands areas were then determined from a Gaussian−Lorenzian fitting using the Labspec 5 software. For experiments performed with samples heated at various temperatures, heat treatment was directly carried out in the μ-Raman apparatus by using a Linkam TS1500 hot stage cooled by a water flow. The sample was placed in a platinum crucible and brought to the chosen temperature at a rate of 50 °C·min^{-1}. After thermal stabilization for 15 min at the given temperature, the sample was cooled down in order to record the μ-Raman spectra at room temperature, thus avoiding blackbody radiation disturbances.

SEM. SEM observations were performed with a FEI Quanta 200 environmental scanning electron microscope (ESEM) using a field-emission gun. Optimal imaging conditions were determined for each compound, leading to the use of different detectors (LFD, large-field detector under low vacuum, or BSED, back-scattering electron detector under high vacuum) and various settings of acceleration voltage (typically between 8 and 15 kV) and working distance (5−9 mm).

EDS. At the same time, the precise mole ratios of cations, x, in $Ce^{IV}_{1-x}Ln^{III}_xO_{2-x/2}$ mixed oxides were determined from energy-dispersive spectrometry (EDS) analyses coupled with the SEM device using a Bruker AXS X-Flash 5010 detector. Prior to making such analyses, each sample was sintered for 10 h at 1400 °C in air, then embedded in an epoxy resin, polished to the 1 μm grid, and carbon coated. EDS results were then obtained from at least 12 different analyses (20 for polyphasic samples). At least 400 000 counts spectra were collected by the EDS detector using an optimal working distance of 11.4 mm and an acceleration voltage of 15 kV.

3. RESULTS AND DISCUSSION

3.1. Characterization and Conversion of Precursors.

Chemical analysis. The stoichiometry of the mixed oxides obtained after heat treatment was evaluated by EDS and compared to that expected from the initial quantities of cerium and lanthanide introduced in the starting mixture (Table 1). The comparison of both expected and experimental ratios is plotted in Figure 1 for $Ce_{1-x}Nd_xO_{2-x/2}$ series. For single-phase samples, successive analyses always showed a weak dispersion of the x_{Ln} values, meaning that these solid solutions were homogeneous. Therefore, taking into account the uncertainty linked to the apparatus, the average x values determined for each compound were assumed to have an absolute accuracy of ±0.005. Moreover, the good agreement between calculated and experimental values (along the first bisector straight line) clearly confirms that both Ce and Nd were quantitatively precipitated as lanthanide oxalates and then converted to the expected mixed oxides by heating. Indeed, only slight composition deviations were noticed and were mainly correlated to uncertainties associated to the EDS measurements and/or to the hygroscopic behavior of the starting lanthanide salts. The reproducibility of the precipitation method was also checked for several chemical compositions examined and led to less than 1% of deviation between replicates. Moreover, the results gathered in Table 1 show that only slight deviations of chemical compositions were also observed for the other $Ce_{1-x}Ln_xO_{2-x/2}$ series compared to the calculated values. In these conditions, oxalic precipitation appeared to be quantitative whatever the trivalent lanthanide ion considered.

Oxalate to Oxide Conversion. TG/DT analyses were performed in order to determine the hydration rate of the oxalate precursors and to underline the chemical reactions occurring during conversion leading to lanthanide oxides for several Ce/Nd mixed samples (with x_{Nd} = 0, 0.285, 0.59, 0.765, and 1). For

dx.doi.org/10.1021/ic200751m |*Inorg. Chem.* 2011, 50, 7150–7161

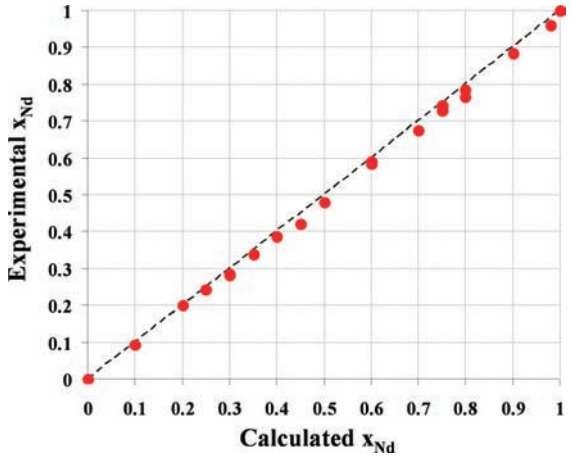

Figure 1. Variation of experimental x_{Nd} mole ratio determined by EDS versus the expected values (corresponding to the initial lanthanides quantities in the starting mixture). The gray dashed line represents the first bisector (i.e., experimental x_{Nd} = expected x_{Nd}).

each compound, two successive water losses were observed (Table 2). The first one (endothermic) occurred between 60 and 250 °C and was associated to the loss of 5−9 water molecules depending on the sample considered. The second weight loss was located between 250 and 350 °C depending on the initial x_{Nd} mole ratio and was associated to loss of one additional water molecule. Finally, the hydration rate of the initial oxalate precursors was found to range from 6 to 10 water molecules depending on the initial composition, which agrees well with the results obtained from XRD characterization.[51]

Thermal conversion leading from anhydrous oxalate to oxide was found to be associated with oxidation of Ce^{3+} into Ce^{4+}. For low x_{Nd} values (up to $x = 0.59$), the transformation occurred in a single step and can be written

$$Ce_{1-x}Nd_x(C_2O_4)_{1.5} \rightarrow Ce_{1-x}Nd_xO_{2-x/2} + (2-x/2)CO\uparrow + (1+x/2)CO_2\uparrow \quad (5)$$

For higher x_{Nd} values, the oxalate decomposition occurred in two steps, which might indicate partial formation of carbonate or oxo−carbonate intermediate(s), as already observed during thermal decomposition of lanthanide oxalate by coupling TG/DT experiments with IR spectroscopy.[55,56] Moreover, the oxalate decomposition temperature increased along with x_{Nd} from about 310 °C for $Ce(C_2O_4)_{1.5}\cdot 4H_2O$ to 600 °C for $Nd(C_2O_4)_{1.5}\cdot 5H_2O$.

Microstructural Characterization. SEM micrographs of several $Ce_{1-x}Nd_x(C_2O_4)_{1.5}\cdot y\ H_2O$ oxalates (with $x = 0$, 0.285, 0.590, 0.765, and 1 and $3 \leq y \leq 5$) and of corresponding mixed oxides are presented in Figure 2. The fast mixing of the solutions containing the reagents led to formation of slat or needle-shape precipitates for all oxalate precursors observed. These grains exhibited an average length of a few micrometers, while their thicknesses reached about 100 nm.

Direct comparison of the morphology of the oxide powders obtained after heating at 1000 °C with that of the initial oxalate precursors showed that such morphology was generally maintained during thermal conversion, proving that the oxalate to oxide conversion could be described as a pseudomorphic transformation.

Micrometric slat-shape aggregates were formed for CeO_2 and $Ce_{0.715}Nd_{0.285}O_{1.86}$, while for higher x_{Nd} values, the mixed oxides adopted a square-plate shape. However, for $x_{Nd} = 0.765$, the thin slats initially formed turned into cubic aggregates (not shown) which could be linked to the separation of the single phase mixed oxalate in two mixed-oxide structures. This point was determined by μ-Raman and XRD (see following sections) and through SEM observation of the surface of a sintered $Ce_{0.235}Nd_{0.765}O_{1.62}$ pellet (Figure 2) where two different phases were clearly evidenced.

From examination of lanthanide oxides micrographs (Figure 2, right column), all oxides prepared were found to be formed by agglomeration of nanometric crystallites. XRD patterns were then used to determine the average size of such crystallites through application of the Scherrer formula[57] on the seven more intense and independent reflections of the $Ia\bar{3}$ and $Fm\bar{3}m$ structures that are (111), (200), (220), (311), (400), (331), and (420) planes for $Fm\bar{3}m$ structure (Miller indices have to be doubled in the case of the $Ia\bar{3}$ structure). The average crystallite sizes were then found to range between 30 and 90 nm depending on the composition but did not appeared to be strongly affected neither by Ln^{III} incorporation nor by the crystal structure of the samples prepared.

3.2. Cerium−Neodymium Mixed Oxides. *XRD Characterization.* XRD patterns of $Ce_{1-x}Nd_xO_{2-x/2}$ mixed oxides prepared via oxalate precipitation are gathered in Figure 3. The XRD diagram of pure CeO_2 only showed the characteristic lines of the fluorite structure ($Fm\bar{3}m$) according to JCPDS File 01-081-0792. The XRD patterns remained unchanged for $x_{Nd} \leq 0.39$, showing that neodymium incorporation did not modify the symmetry of the crystal in this range of composition. On the contrary, additional XRD lines were observed for $x_{Nd} \geq 0.42$ (at about 20°, 34.5°, 38.5°, 42°, and 51° as pointed out by the asterisks in Figure 3), which accounted for formation of the cubic $Ia\bar{3}$ superstructure [JCPDS file 00-028-0267].[58−60]

The structural modifications occurring during Ln^{III} loading are illustrated through the description of F- and C-type structural types (Figure 4). First, Figure 4a represents the typical fluorite structure, the cations being drawn as green atoms surrounded in a cubic environment by eight oxygen atoms (represented in red). In the F structure, the oxygen vacancies, created along with substitution of Ce^{IV} by Ln^{III}, are randomly located by occupying oxygen sites. On the contrary, the increase of incorporation rate leads to their ordering, thereby to the C-type superstructure. This structure can then be built by replacing one oxygen atom by one vacancy at each of the four positions along the [111] direction from the fluorite unit cell[60−63] and by displacing the cations located at the center of the faces in the cubic fluorite cell to a new crystallographic site (24d Wyckoff site, corresponding to the blue spheres in Figure 4b and 4c). These modifications lead to the description of the new structure through the doubling of the unit cell size, i.e., to an assembly of eight unit cells of the initial fluorite structure.

In order to follow more easily the variations of the unit cell parameters during incorporation of trivalent lanthanide elements, the values reported in Table 1 thus correspond to the a parameter for the fluorite structure and to $a/2$ for the C-type phase.

Looking back at Figure 3, observation of supplementary XRD lines for $x_{Nd} \geq 0.73$ indicated the presence of a two-phase system composed by the C-type compound and additional A-type Nd_2O_3 [hexagonal, space group $P\bar{3}1m$, JCPDS file 00-043-1023]. The unit cell of the latter is depicted in Figure 4d. The contribution of this A-type phase to the XRD patterns increased with x_{Nd} up to pure neodymium sesquioxide. This additional

dx.doi.org/10.1021/ic200751m |*Inorg. Chem.* 2011, 50, 7150–7161

Table 2. Results of DTA/TGA Experiments Associated with the Oxalate to Oxide Conversion

	x_{Nd} (experimental, determined by EDS)				
	0.000	0.285	0.590	0.765	1.000
first water loss					
number of involved H_2O	7	9	5	7	9
temp. range (°C)	80−200	100−200	70−250	60−220	70−250
second water loss					
number of involved H_2O	1	1	1	1	1
temp. range (°C)	230−290	250−320	260−350	290−380	320−380
total hydration number $2y$	8	10	6	8	10
temp. range of oxalate/oxide conversion (°C)	280−340	330−390	370−450	390−500[a]	390−660[a]
temp. at maximum heat flow (°C)	310	370	410	410 and 450[a]	550 and 640[a]

[a] Oxalate to oxide conversion observed in two steps.

phase was also pointed out on the SEM micrographs of sintered $Ce_{0.235}Nd_{0.765}O_{1.62}$ pellets (Figure 2), where it lied along grain boundaries of the main C phase.

Moreover, the variation of the unit cell parameter of $Ce_{1-x}Nd_xO_{2-x/2}$ mixed oxides versus x clearly exhibited the appearance of a maximum value above $x = 0.72$ (Figure 5), which was correlated to the solubility limit of neodymium in CeO_2. Similarly, the refined unit cell parameters determined for the A-type phase remained close to that of pure Nd_2O_3, thus indicating a very weak incorporation of cerium in this phase.

μ-Raman Characterization. Besides XRD characterization, further exploration of $Ce_{1-x}Nd_xO_{2-x/2}$ samples was carried out by μ-Raman spectroscopy (Figure 6). In ceria F- and C-type host structures, it is well established that incorporation of a trivalent element is accompanied by formation of one-half an oxygen vacancy for each Ce^{IV} ion substituted with respect to the charge balance. As first reported by McBride et al.,[64] Raman spectroscopy allows studying the cations−oxygen bonds in $Ce_{1-x}Ln_xO_{2-x/2}$ samples and is thus particularly convenient to point out the presence of oxygen vacancies.

In order to compare the variation of μ-Raman band intensities observed when increasing the neodymium loading x_{Nd}, all spectra were normalized to get the same intensity for the 465 cm^{-1} band (except for the pure Nd_2O_3 spectrum in which this band was not observed). Indeed, the latter was the only band observed in the Raman spectrum of CeO_2. It corresponds to the F_{2g} vibration mode of the M−O bond when the cation is surrounded by eight oxygen atoms.[64,65]

A shift toward lower wavenumbers of the F_{2g} band from 461 (CeO_2) to 453 cm^{-1} ($Ce_{0.61}Nd_{0.39}O_{1.805}$) with increasing mole ratio x_{Nd} in the F-type solid solutions was observed. The same tendency was also observed for the C-type solid solutions as the F_{2g} band varied from 466 ($Ce_{0.58}Nd_{0.42}O_{1.79}$) to 452 cm^{-1} ($Ce_{0.215}Nd_{0.785}O_{1.61}$). Some authors mentioned the decrease of M−O distance in fluorite-type $Ce_{1-x}Ln_xO_{2-x/2}$ from X-ray absorption fine structure (XAFS) results when increasing the Ln^{III} content.[66,67] This diminution could thus be linked to contraction of M−O bonds.

Besides, an important shift toward the higher wavenumber values was observed between $Ce_{0.61}Nd_{0.39}O_{1.805}$ (453 cm^{-1}) and $Ce_{0.58}Nd_{0.42}O_{1.79}$ (466 cm^{-1}) spectra. It was likely assigned to the transition from the F-type to the C-type structure.

Supplementary bands appeared when increasing the neodymium content. In particular, the broad band located at around 580 cm^{-1} was assigned to the M−O A_{1g} and F_{2g} vibration modes but with M surrounded by at least one oxygen vacancy.[64−69] The observation of this vibration mode was always correlated to that of an unreferenced band for $Ce_{1-x}Ln_xO_{2-x/2}$ at about 275 cm^{-1}, which followed the same trend in intensity. This band is consistent with that observed at 260 cm^{-1} (A_{1g}) from polarized Raman experiments on $Ce_{1-x}Y_xO_{2-x/2}$ compounds by Nakajima et al.[68] which they correlated to the presence of oxygen vacancies. Furthermore, when the neodymium amount increased in solid solutions, the relative intensity of both 275 and 580 cm^{-1} bands increased compared to the F_{2g} band, confirming the progressive incorporation of trivalent lanthanide through coupled formation of oxygen vacancies.[4,16]

The additional band detected at 370 cm^{-1} for $0.42 \leq x_{Nd} \leq 0.965$ is usually reported as a vibration mode for the cubic Ln_2O_3 C-type structure.[26,27] This band was observed all along the field of existence of the C-type structure in $Ce_{1-x}Nd_xO_{2-x/2}$ (determined from XRD). It was thus correlated to the presence of the $Ia\bar{3}$ superstructure and was probably linked to formation of a second cationic site in the C-type structure as enlightened in Figure 4c. Formation of the C-type structure also appeared to be linked with the observation of a shoulder on the 580 cm^{-1} broad band associated to oxygen vacancies.

Whatever the additional band considered, these characteristic vibration modes for the C-type structure were also weakly observed for $x_{Nd} = 0.39$, which was found to belong to the F-type structure from XRD patterns. This discrepancy was already reported by Mandal et al.[26] during their study of the $Ce_{1-x}Er_xO_{2-x/2}$ mixed oxides and underlined the sensitivity of μ-Raman spectroscopy to detect weak amounts or subnanometric phase domains of C-type phase compared to other techniques such as XRD.

Finally, for the highest x_{Nd} contents, Nd_2O_3 related bands appeared at 320, 430, and 480 cm^{-1}, which agreed well with the spectrum recorded by Denning et al.[70] using a similar incident laser wavelength (633 nm He−Ne radiation). Although the A-type phase amount was very low (probably less than 1 wt %) in the mixture obtained for $x_{Nd} = 0.73$ (Figure 3), the band centered at 320 cm^{-1} was easily observed, showing again the high sensitivity of μ-Raman spectroscopy regarding to the presence of Nd_2O_3 in the prepared samples.

Limits of Incorporation of Nd in F- and C-Type Ceria. Several authors determined the solubility limit of Nd in the C-type CeO_2 structure. On this basis, the value obtained in this work ($x_{Nd} \approx 0.73$) appeared in good agreement with the results reported by Ikuma

dx.doi.org/10.1021/ic200751m |Inorg. Chem. 2011, 50, 7150–7161

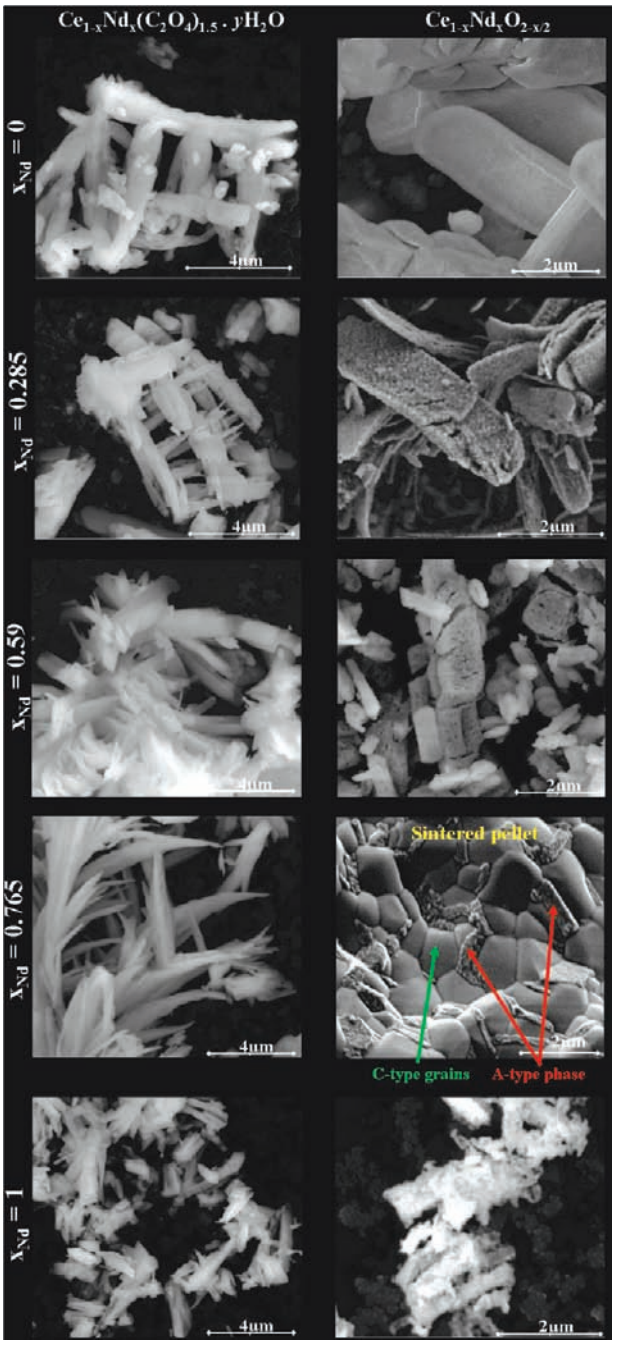

Figure 2. SEM micrographs of powdered Ce/Nd oxalates and of the corresponding oxides. The image of sintered $Ce_{0.235}Nd_{0.765}O_{1.62}$ pellet shows the presence of two phases: Nd_2O_3 (A-type) being present along grain boundaries of the C-type phase.

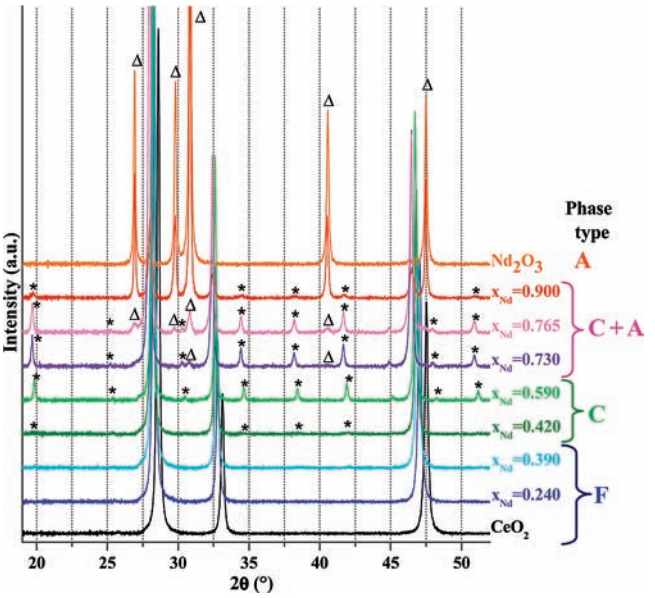

Figure 3. XRD patterns obtained for the $Ce_{1-x}Nd_xO_{2-x/2}$ series. **F** = F-type $Fm\bar{3}m$ structure, **C** = C-type $Ia\bar{3}$ structure, and **A** = A-type $P\bar{3}1m$ structure (Nd_2O_3). Additional main XRD lines assigned to the C-type (*) and A-type (**Δ**) structures are pointed out.

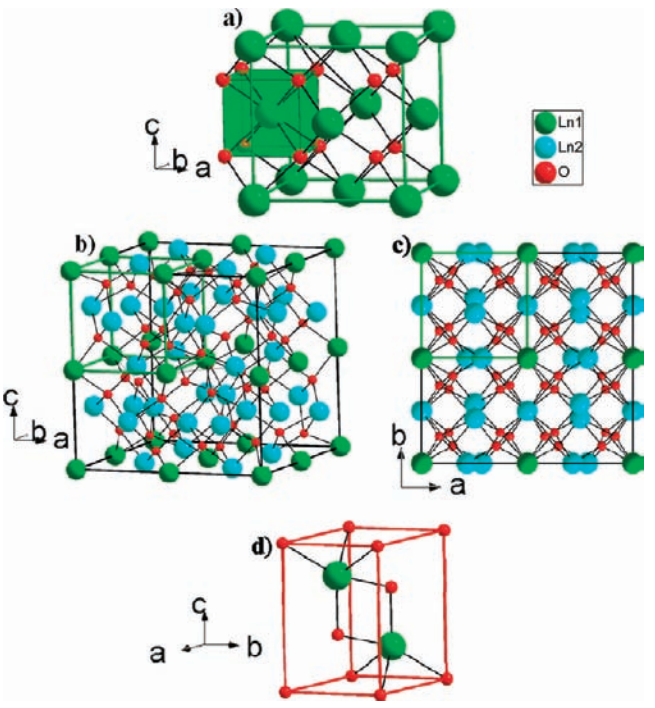

Figure 4. Perspective view of F-type unit cell (a) compared with C-type structure (b) and its projection along the *c* axis (c). In C-type structure, Ln1 green spheres denotes 8b Wyckoff positions while Ln2 blue ones shows 24d positions.[60] (d) Unit cell of A-type crystalline structure.

et al.[18] (x_{Nd} = 0.75) and by Chavan et al.[20] (x_{Nd} = 0.70) despite the significant differences in the chemical ways of preparation (ammonia coprecipitation followed by a calcination step at 800 °C in air and the solid state route from CeO_2 and Nd_2O_3 mixture heated at 1400 °C, respectively). Moreover, on the basis of our results, the limit reported by Nitani et al.[22] (x_{Nd} = 0.6), who also used a solid-state route from CeO_2 and Nd_2O_3, diverged significantly probably because of a heterogeneous distribution of the cations in the sample. On the contrary, the synthesis routes involving coprecipitated precursors similar to that employed in the present study usually led to a homogeneous cationic distribution and then to a maximal solubility of neodymium in the CeO_2 structure.

On the other hand, Ikuma et al.[18] and Hagiwara et al.[21] reported a transition between F- and C-type structures for $0.40 \leq x_{Nd} \leq 0.45$, which was close to the limit determined in

dx.doi.org/10.1021/ic200751m |*Inorg. Chem.* 2011, 50, 7150–7161

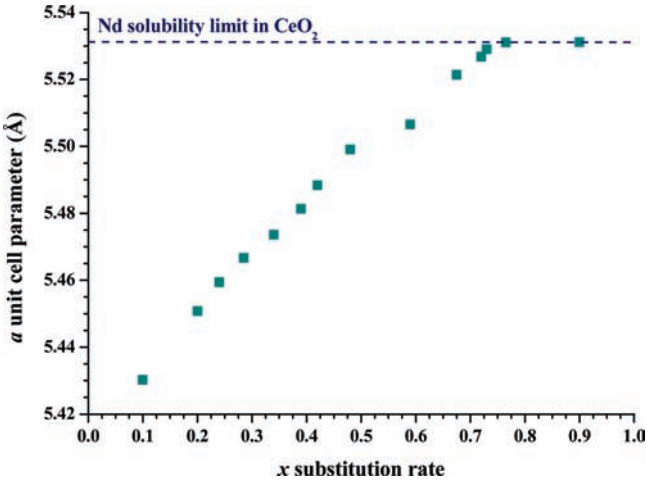

Figure 5. Variation of $Ce_{1-x}Nd_xO_{2-x/2}$ unit cell parameter versus x_{Nd} substitution rate.

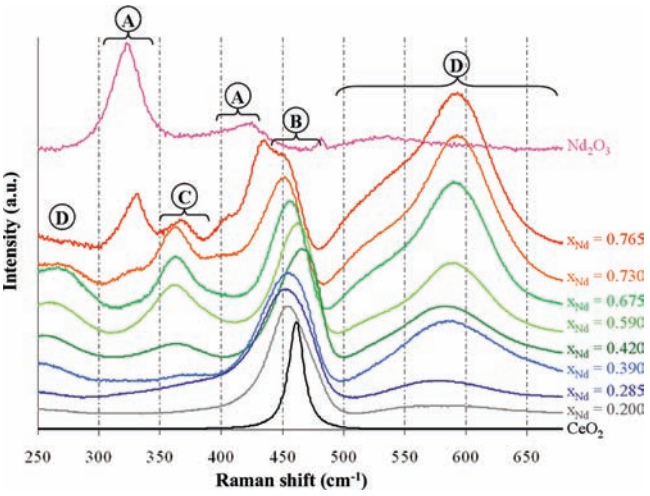

Figure 6. μ-Raman spectra recorded for $Ce_{1-x}Nd_xO_{2-x/2}$ samples. Surrounded letters denote **A** A-type Nd_2O_3 characteristic bands,[70] **B** ν_{M-O} F_{2g} Raman mode of CeO_2 fluorite, **C** C-type structure related band, and **D** ν_{M-O} band with M surrounded by at least one oxygen vacancy.

this work ($0.39 \leq x_{Nd} \leq 0.42$). However, Chavan et al.[20] reported this transition to occur for $0.500 \leq x_{Nd} \leq 0.525$, while Nitani et al.[22] obtained a mixture of both F- and C-type structures for $x_{Nd} = 0.40$. Once again, these differences could be associated to some cationic heterogeneity resulting from the solid state elaboration route.

In addition to the synthesis route, heat treatment seemed to have a great influence on both C- and F-type stability ranges for $Ce_{1-x}Ln_xO_{2-x/2}$ systems. In order to shed light on its role, samples of $Ce_{0.61}Nd_{0.39}(C_2O_4)_{1.5}\cdot 3H_2O$ (oxalate precursor of the F-type oxide) and $Ce_{0.27}Nd_{0.73}(C_2O_4)_{1.5}\cdot 4H_2O$ (oxalate precursor of the C-type oxide) were heated between 600 and 1400 °C for 1 h and then analyzed by XRD at room temperature. Since the main objective was to examine formation of the C-type form for $Ce_{0.61}Nd_{0.39}O_{1.805}$ and of the A-type form for $Ce_{0.27}Nd_{0.73}O_{1.635}$, XRD measurements were focused in the domains of interest corresponding to the strongest XRD lines of both structures.

Besides, μ-Raman spectroscopy was also used to evidence the effects of the heating temperature for three compositions: $x_{Nd} = 0.39$ and 0.59 in order to check formation of the C-type superstructure, on the one hand, and $x_{Nd} = 0.73$ to determine the sensitivity of Nd solubility in the C-type phase toward temperature, on the other.

XRD patterns obtained for $Ce_{0.27}Nd_{0.73}O_{1.635}$ (Figure 7b) revealed the presence of weak XRD lines corresponding to the A-type form between 600 and 1000 °C. On the contrary, they were clearly observed at 1200 °C and then disappeared at 1400 °C.

μ-Raman spectra confirmed these results (Figure 7a) and allowed pointing out more accurately the temperature of formation of the A-type phase. Indeed, the characteristic Raman band of this latter phase (located near 330 cm^{-1}) clearly appeared above 800 °C. Its relative intensity compared to the F_{2g} vibration band was then found to be almost constant up to 1000 °C and then started to decrease, correlating to the possible extension of Nd stabilization in the C-type solid solution for the highest temperatures of heat treatment.

Direct comparison of both techniques involved showed small discrepancies coming from various conditions of heat treatment (heating and cooling rates, holding time). It also suggested that μ-Raman spectroscopy was used as an advantage to detect smaller phase amounts than XRD. Thereby, domains of the A-type phase were probably formed at 800 °C with the heat treatment conditions applied for μ-Raman experiments and remained stable up to 1400 °C.

The relative stability limit between the F- and C-type structures was also studied as a function of heating temperature. As the C-type structure results in an ordering of oxygen vacancies in the fluorite lattice, the irreversible phase transition from the F-type to the more ordered C-type structure was examined by μ-Raman spectroscopy at high temperature for $x_{Nd} = 0.39$, i.e., close to the limit determined between both structures at 1000 °C (Figure 8). The relative intensity of the band associated to this structure (located at 370 cm^{-1}) increased between 700 and 900 °C and then remained stable up to 1400 °C. Similar results were also obtained for $x_{Nd} = 0.59$ with a progressive increase of the 370 cm^{-1} band between 600 and 1100 °C (see Supporting Information).

For the three compounds studied, the results evidenced that formation of the superstructure, thus ordering of oxygen vacancies, was thermally activated. Moreover, the μ-Raman study between 500 and 1000 °C systematically revealed a progressive shift of the F_{2g} band to the upper wavenumbers associated to its progressive narrowing, which was generally linked to an increase of the crystallinity of these samples with temperature.

The results of μ-Raman experiments concerning the temperature dependence of the F/C and C/C+A phase transitions for $Ce_{1-x}Nd_xO_{2-x/2}$ solid solutions produced via oxalic homogeneous precursors are summarized in Table 3. The fluorite-type structure remained stable at low temperature even for high Nd content, proving that the ordering of oxygen vacancies associated to formation of C-type structure was thermally activated. Formation of additional A-type phase appeared above 800 °C for $Ce_{0.27}Nd_{0.73}O_{1.635}$, which clearly underlined the effect of temperature on this second limit.

However, the heating temperature could be also responsible for some modifications in the crystalline structures stability range and in the solubility limits essentially through the increase of crystallites sizes induced by heat treatment. Indeed, it was proved for other mixed systems that the solubility limit of an element in a solid solution could be shifted by the size[71,72] or even the shape[73]

dx.doi.org/10.1021/ic200751m |Inorg. Chem. 2011, 50, 7150–7161

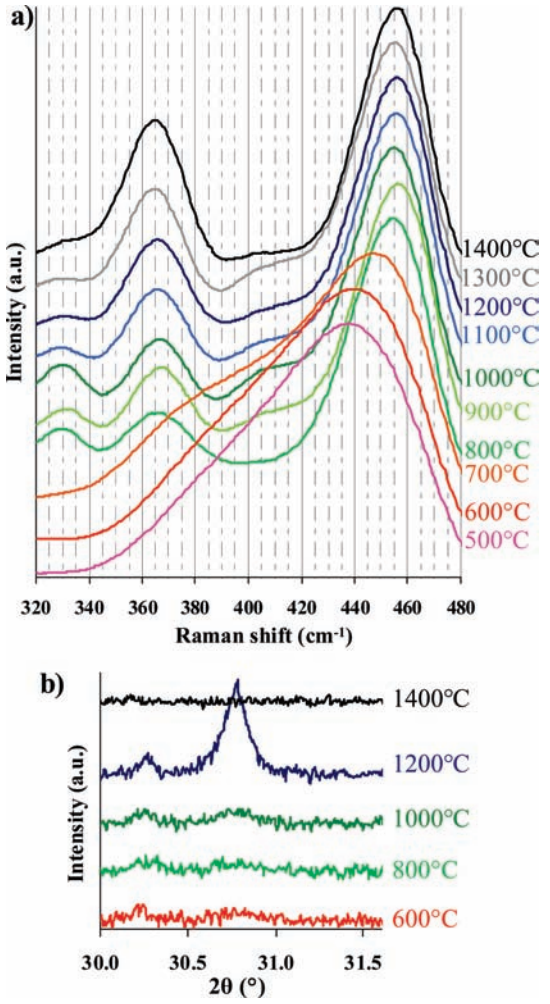

Figure 7. μ-Raman spectra (a) and XRD (b) of $Ce_{0.27}Nd_{0.73}O_{1.635}$ for several heating temperatures (500 °C ≤ T ≤ 1400 °C).

of the crystallites. Thus, in this study, both heat treatment and crystallite size parameters could be responsible for the observed extended solubility of Nd in the cubic phase of $Ce_{0.27}Nd_{0.73}O_{1.635}$ below 800 °C.

3.3. Cerium Lanthanide Mixed Oxides: Variation of Unit Cell Parameters. *Cerium−Erbium Oxide Solid Solutions.* In order to compare the effect of incorporation of heavy rare-earth element (thus exhibiting smaller cationic radii) in the CeO_2 structure with that of a light REE such as neodymium, samples of $Ce_{1-x}Er_xO_{2-x/2}$ solid solutions were prepared and then characterized through XRD in the same way as the $Ce_{1-x}Nd_xO_{2-x/2}$ series (Table 1). From XRD patterns, erbium-doped ceria samples were found to adopt the fluorite structure for $x_{Er} \leq 0.29$. The ordering of oxygen vacancies occurred for higher erbium amounts ($x_{Er} \geq 0.39$), leading to formation of the C-type structure. As this structural organization also corresponds to the stable form of Er_2O_3, it was found to be maintained in the whole range of composition ($0.39 \leq x_{Er} \leq 1$).

Moreover, the samples were always found to be monophasic, conversely to the data reported by Mandal et al.,[27] who argued on formation of a two-phase system composed by the F- and C-types solid solutions. Since the main XRD lines of the F-type structure overlapped with the main ones of the C-type structure, accurate analysis of the XRD lines corresponding to the (022) and (311) planes (respectively, the (044) and (622) planes for

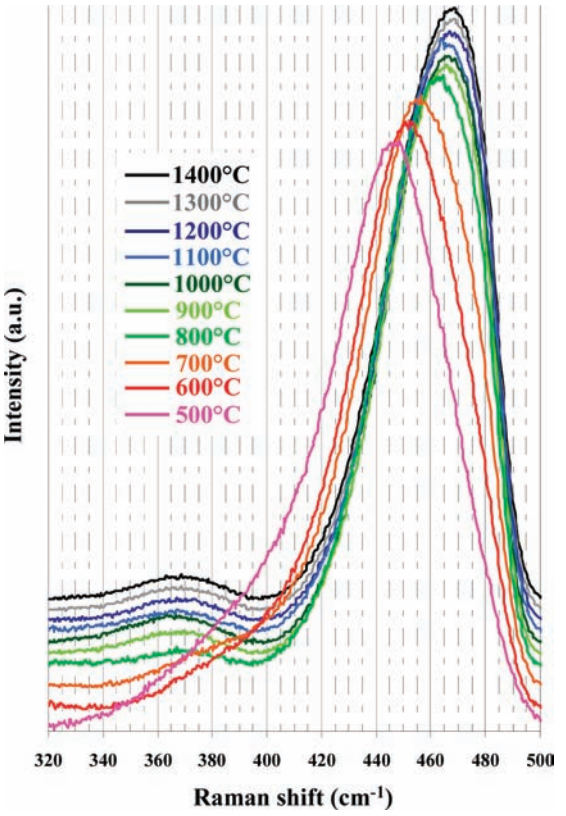

Figure 8. μ-Raman spectra of $Ce_{0.61}Nd_{0.39}O_{1.805}$ for heating temperatures ranging from 500 (bottom) to 1400 °C (top).

Table 3. Field of Existence of $Ce_{1-x}Nd_xO_{2-x/2}$ Crystalline Structures Determined from μ-Raman Experiments As a Function of Temperature of Heat Treatment

	composition of mixed oxides		
heating temp. (°C)	$Ce_{0.61}Nd_{0.39}O_{1.805}$	$Ce_{0.41}Nd_{0.59}O_{1.705}$	$Ce_{0.27}Nd_{0.73}O_{1.635}$
500	F	F	F
600	F	F	F
700	C	C	C
800−1400	C	C	C+A

C-type) was carried out for several $Ce_{1-x}Er_xO_{2-x/2}$ samples (x_{Er} = 0.39, 0.595, and 0.745) in order to check the proposed assumption (Figure 9). Such XRD lines were particularly examined since they were intense and expected to split in two components in the case of a phase separation. Nevertheless, the symmetric shape of the peaks unambiguously confirmed that only single-phase $Ce_{1-x}Er_xO_{2-x/2}$ solid solutions were prepared in the whole composition range for the oxalate precipitation route, confirming the interest of such chemical route to prepare homogeneous and single-phase mixed oxides.

Lanthanum-, Samarium-, Europium-, Gadolinium-, Dysprosium-, and Ytterbium-Based Compounds. In order to generalize both studies, several samples with the general chemical composition $Ce_{0.90}Ln_{0.10}O_{1.95}$, $Ce_{0.70}Ln_{0.30}O_{1.85}$, $Ce_{0.40}Ln_{0.60}O_{1.70}$, and Ln_2O_3 were prepared with various trivalent lanthanide elements (Ln = La, Sm, Eu, Gd, Dy, or Yb) and then characterized through

dx.doi.org/10.1021/ic200751m |*Inorg. Chem.* 2011, 50, 7150–7161

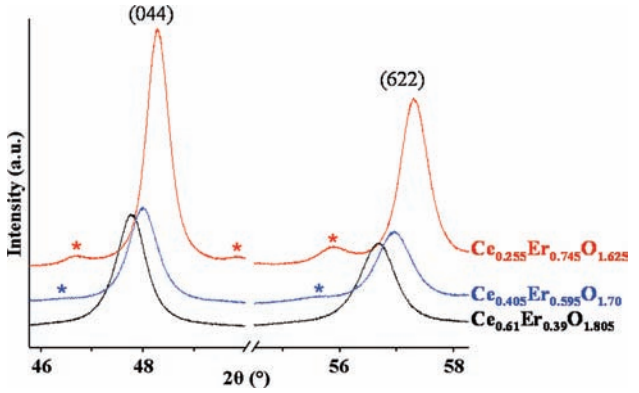

Figure 9. Analysis of the (044) and (622) XRD lines of $Ce_{1-x}Er_xO_{2-x/2}$ samples (x_{Er} = 0.39, 0.595, and 0.745). Characteristic lines of C-type superstructure are pointed out by asterisks (*).

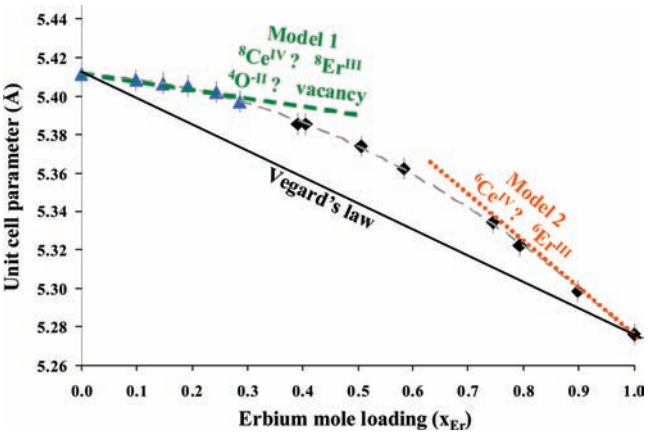

Figure 10. Variation of the experimental unit cell parameters of $Ce_{1-x}Er_xO_{2-x/2}$ versus the erbium mole loading (x_{Er}). Blue triangles refers to F-type samples ($x_{Er} \leq 0.29$), while black diamonds refer to $a/2$ values for C-type samples ($x_{Er} \geq 0.39$). Gray dotted line corresponds to the result of fitting taking into account a quadratic function. The representation of Vegard's law (straight black line) as well as the expression of both models described are also reported.

EDS (Table 1) and XRD. The XRD patterns of $Ce_{0.40}Ln_{0.60}O_{1.70}$ are reported as Supporting Information. For $x_{Ln} \approx 0.10$ and 0.30, all samples exhibited the fluorite-type structure from lanthanum to ytterbium. Conversely, samples with the general composition $Ce_{0.40}Ln_{0.60}O_{1.70}$ were found to crystallize with the C-type structure, except for $Ce_{0.41}La_{0.59}O_{1.70}$ where the F-type phase was maintained[27,30,36,74,75] and for $Ce_{0.40}Yb_{0.60}O_{1.70}$ which was the only composition leading to a mixture of two C-type structures (as evidenced by the split of all XRD lines of this pattern). Additionally, the lanthanide sesquioxides were found to crystallize with the C-type structure from Eu_2O_3 to Yb_2O_3. Moreover, Sm_2O_3 was obtained with a monoclinic structure, while Nd_2O_3 and La_2O_3 kept the A-type structure.

Unit Cell Parameter Variation in the $Ce_{1-x}Ln_xO_{2-x/2}$ Series. While formation of a solid solution should suggest a linear trend when plotting the unit cell parameters of $Ce_{1-x}Ln_xO_{2-x/2}$ compounds versus the x substitution rate, the variation of the lattice parameters of $Ce_{1-x}Er_xO_{2-x/2}$ samples (Figure 10) obviously followed a polynomial law as already reported for others in the $Ce_{1-x}Ln_xO_{2-x/2}$ series. Bevan et al.[75] first proposed to fit this variation according to the following quadratic function

$$a = Ax_{Er^3} + Bx_{Er} + C \quad (6)$$

where a is the unit cell parameter (expressed in Angstroms) and A, B, and C are three parameters obtained from the fitting of experimental results.

On the basis of XAFS measurements[22,66,67] and molecular dynamics calculations,[76] some authors reported that the shrinkage of Ce−O or Ln−O bond lengths and the decrease of oxygen/oxygen repulsions in the structure led to nonlinear contraction of the unit cell.

Besides, construction of a $Ce^{IV}{}_{1-x}Er^{III}{}_xO_{2-x/2}$ solid solution from CeO_2 could be described as a progressive substitution of $^{(8)}Ce^{IV}$ ions (i.e., Ce^{4+} ion in an cubic environment) by $^{(8)}Er^{III}$ ions. Along with this cationic substitution, replacement of $^{(4)}O^{2-}$ ions by oxygen vacancies must be also considered. On the basis of this point, a theoretical variation of the unit cell parameter was calculated using an ion-packing model, as already proposed by Hong and Virkar,[19] i.e.

$$a_{model1} = k_1\frac{4}{\sqrt{3}}\left[R_{^{(8)}Er^{III}} + (1-x_{Er})R_{^{(8)}Ce^{IV}} + (1-0.25x_{Er})R_{(4)_{O^{-II}}} + 0.25x_{Er}R_{(4)_{V_O}}\right] \quad (7)$$

where $R_{(4)V_O}$ is the estimated ionic radius of an oxygen vacancy determined by Hong and Virkar[19] (1.164 Å), the other R_i symbols denote the ionic radii from Shannon's table[10] (1.00, 0.97, and 1.38 Å for $^{(8)}Er^{III}$, $^{(8)}Ce^{IV}$, and $^{(4)}O^{-II}$, respectively), and k_1 is a factor used to correct the uncertainties coming from the accuracy of ionic radius values (here k_1 = 0.9971[19]). Calculation of this function led to the dotted green line presented in Figure 10. The results of this function fitted well with low erbium mole loadings and then diverged from the experimental results from x_{Er} = 0.285 and for higher mole loadings because this model did not take into account neither the transition to the C-type structure nor the decrease of coordination numbers of erbium and cerium ions from 8 to 6 with increasing x_{Er}.

On the other hand, the second model considered started from a C-type Er_2O_3 structure which would fit the unit cell parameter of the solid solution for the composition range $0.745 \leq x_{Er} \leq 1$, as drawn by the dotted orange line in Figure 10. Similar to model 1, it could be considered at high x_{Er} that Ce^{IV} ions were inserted in Er_2O_3 with a coordination number of 6 along with addition of oxygen ions. Since the ion-packing model could not deal with the effect of oxygen insertion in the C-type structure, this second model was not applicable. The combination of both linear models could fit in a better way the experimental variation of the unit cell parameters and explain their deviation from the Vegard law. Finally, even if the variation of the a parameter versus x_{Er} did not respect Vegard's law,[77,78] it remained compatible with formation of single-phase solid solutions as evidenced for other mixed systems, such as $(Ga_{1-x}Zn_x)(N_{1-x}O_x)$[79] or $Ba_xSr_{1-x}SO_4$.[80] It also confirmed formation of single-phase compounds on the whole range of composition instead of mixtures of F- and C-type structures.

The variation of the unit cell parameters obtained for all $Ce_{1-x}Ln_xO_{2-x/2}$ solid solutions (Ln = Nd, Sm, Eu, Gd, Dy, and Er) examined are gathered in Figure 11. In order to underline more evidently the effects of incorporation of the studied rare-earth elements, the variation of the unit cell parameter was plotted versus the average ionic radii of cations R_{iA}[10] calculated

dx.doi.org/10.1021/ic200751m |Inorg. Chem. 2011, 50, 7150–7161

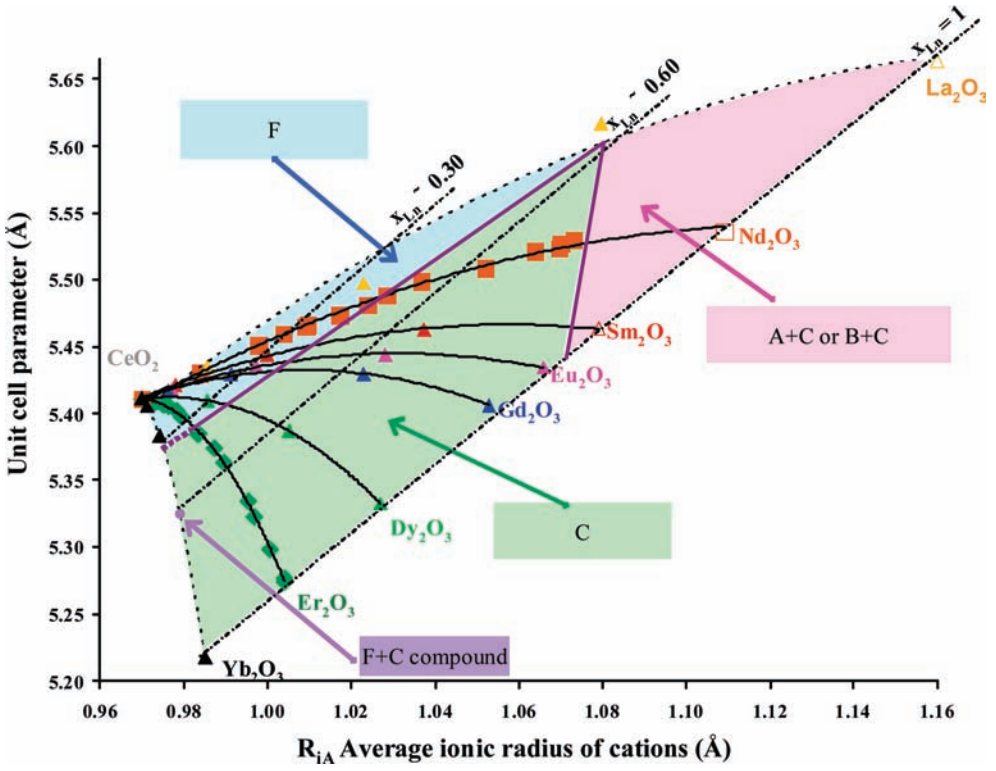

Figure 11. Variation of the unit cell parameters of $Ce_{1-x}Ln_xO_{2-x/2}$ versus the calculated average cationic radius in the structure. Solid black lines result from the fitting reported in Table 4. Dotted lines denote the tendencies observed for a given substitution ratio of cerium in $Ce_{1-x}Ln_xO_{2-x/2}$.

Table 4. Results of Fitting of the Unit-Cell Parameters Variation for $Ce_{1-x}Ln_xO_{2-x/2}$ Solid Solutions According to Eq 8

loaded Ln^{III}	La	Nd	Sm	Eu	Gd	Dy	Er	Yb
$Ri_{(Ln)}$ in 8-fold coordination[10] (Å)	1.160	1.109	1.079	1.066	1.053	1.027	1.004	0.985
fitted parameters								
A'	3.94	−5.366	−7.126	−8.95	−13.61	−31.46	−105.95	−583.62
B'	−6.20	12.10	15.07	18.46	27.47	61.46	205.14	1128.04
C'	7.72	−1.281	−2.502	−4.072	−8.43	−24.60	−93.886	−539.66

according to eq 4. Due to preparation of polyphasic systems, the data obtained for $Ce_{1-x}Nd_xO_{2-x/2}$ with $x_{Nd} \geq 0.73$ and for $Ce_{0.4}Yb_{0.6}O_{1.7}$ are not reported in Figure 11. Moreover, since we always obtained Sm_2O_3 in the monoclinic form and Nd_2O_3 with the A-type structure, the unit cell parameters reported for the cubic $Ia\bar{3}$ forms were used (JCPDS files 00-043-1029 and 03-065-3184,[81] respectively).

As already evidenced for $Ce_{1-x}Er_xO_{2-x/2}$, the unit cell parameter variations were always correctly fitted by using the following quadratic fitting function

$$a = A' \times R_{iA}^2 + B' \times R_{iA} + C' \qquad (8)$$

The variation of the unit cell parameter of the $Ce_{1-x}Nd_xO_{2-x/2}$ and $Ce_{1-x}Er_xO_{2-x/2}$ series versus average ionic radius was then fitted by means of eq 8, leading to values of the A', B', and C' parameters gathered in Table 4. In order to compare the influence of the trivalent lanthanide cation, indicative values were also proposed for the other $Ce_{1-x}Ln_xO_{2-x/2}$ solid solutions for which only three experimental points were considered (along with CeO_2 and corresponding Ln_2O_3 reference data). Also, it is worth noting that the refinement results from the Ce/La solid solutions were disturbed by the hygroscopic character of La_2O_3,[53,82] leading to greater uncertainties for this series.

On this basis, the variation of the unit cell parameter of $Ce_{1-x}Ln_{2-x/2}$ solid solutions (Figure 11) revealed three different behaviors depending on the considered REE:

- For Ln = La and Nd, the unit cell parameter kept increasing on the whole range of composition while increasing R_{iA} (increasing x_{Ln}).
- For Ln = Sm, Eu, and Gd, the a value first increased up to about $x = 0.6$ and then slightly decreased.
- For Ln = Dy, Er, and Yb, the solid solution lattices shrank continuously from $x = 0$ to $x = 1$.

Such differences were explained through the competition of two opposite effects. The first one, already discussed, laid in the decrease of the O−O repulsion and then tends to contract the unit cell. Conversely, substitution of Ce^{4+} by larger Ln^{3+} cations led to expansion of the lattice. In these conditions, the effect of the oxygen vacancies appeared to be predominant for heavier REE, i.e., from Dy to Lu. On the contrary, as the difference between Ce^{4+} and Nd^{3+} or La^{3+} is greater (see Table 4), the contraction effect due to the oxygen vacancies was not strong enough to counterbalance the cell size increase due to the increase of R_{iA} for these two series.

dx.doi.org/10.1021/ic200751m |Inorg. Chem. 2011, 50, 7150–7161

Furthermore, when comparing the R_{iA} values (Figure 11) with the determined or cited solubility limits of Ln in C-type ceria, it appeared that these limits were driven by steric constraints linked to the average cationic radius. Indeed, from the results obtained for $Ce_{0.27}Nd_{0.73}O_{1.635}$, the limit was obtained for R_{iA} = 1.073 Å. Moreover, the observation of a secondary phase in the $Ce_{1-x}Sm_xO_{2-x/2}$ and $Ce_{1-x}La_xO_{2-x/2}$ series was commonly reported for various synthesis routes, respectively, for about $x_{Sm} = 0.9$[18,24] (i.e., R_{iA} = 1.068 Å) and $x_{La} = 0.5$[23,28,31] (i.e., R_{iA} = 1.065 Å). This showed that this limit mainly depends on steric issues, since it occurred around R_{iA} = 1.07 Å, as evidenced by the limit between C-type and C+A-type domains (Figure 11). Furthermore, it also explained why no additional phase was obtained for the other $Ce_{1-x}Ln_xO_{2-x/2}$ series (from Eu to Yb), since the determined R_{iA} limit value could not be reached for these series even for $x_{Ln} = 1$.

On the contrary, as the transition of the F-type to C-type structure was mainly driven by the amount of oxygen vacancies (which occurs for an Ln^{III} mole loading of about $x_{Ln} \approx 0.4$), this phase limit was not significantly affected by steric effects.

4. CONCLUSION

$Ce_{1-x}Ln_xO_{2-x/2}$ mixed oxides were investigated in order to point out the structural deformations induced by incorporation of aliovalent cations and subsequent formation of oxygen vacancies in the fluorite-type unit cell of the $M^{IV}O_2$ dioxides. Whatever the trivalent lanthanide considered, the initial fluorite structure was found to be stable up to about $x = 0.4$, where rearrangement of oxygen vacancies led to apparition of a cubic superstructure. The stability of the latter versus the substitution rate then strongly depended on the lanthanide considered: while incorporation reached a maximum value for lanthanum, neodymium, and samarium, pure end members were obtained from europium to ytterbium.

A comparison of the values obtained in this study with that previously mentioned in the literature first evidenced the benefits of wet chemistry methods of preparation in terms of cation homogeneity. Indeed, the oxalic coprecipitation used in this work generally led to incorporation rates higher than that usually obtained through solid state chemistry. Also, the joint use of XRD and μ-Raman spectroscopy of the solids allowed us to point out more accurately the stability limits of the various crystal phases considered.

On the basis of these results, the variation of the refined unit cell parameters of $Ce_{1-x}Ln_xO_{2-x/2}$ (Ln = La, Nd, Sm, Eu, Gd, Dy, Er, and Yb) solid solutions versus x was described through a quadratic fitting function. Such experimental data could appear useful for the preparation and characterization of new compositions of $Ce_{1-x}Ln_xO_{2-x/2}$ and/or $An^{IV}{}_{1-x}Ln_xO_{2-x/2}$ (An^{IV} = Th, U) samples, which stand as model oxide fuels.[44−48,83,84]

Furthermore, they could be directly correlated to the modifications of the physicochemical properties of such compounds with chemical composition. Indeed, both deformation of initial unit cell and formation of oxygen vacancies are expected to modify significantly several properties of interest. First, formation of structural defects along with incorporation of trivalent elements could act as a sintering aid through their strong impact on the densification kinetics. These differences as well as that encountered in the structural type stabilized could generate important variations in the final microstructures of the cohesive materials prepared. Finally, the presence of oxygen vacancies could be also of importance when performing leaching tests on such samples. Since they could induce important modifications of lattice cohesion energies, a strong variation of the normalized dissolution rates is expected.

■ ASSOCIATED CONTENT

Supporting Information. XRD and μ-Raman characterization of $Ce_{0.715}Nd_{0.285}(C_2O_4)_{1.5}\cdot 5H_2O$; μ-Raman heat treatment effects study on $Ce_{0.41}Nd_{0.59}O_{1.705}$; XRD patterns of $Ce_{0.4}Ln_{0.6}O_{1.7}$ synthesized oxides. This material is available free of charge via the Internet at http://pubs.acs.org.

■ AUTHOR INFORMATION

Corresponding Author
*E-mail: nicolas.dacheux@icsm.fr.

■ ACKNOWLEDGMENT

The authors would like to thank the MATINEX French Research Group (*Innovative materials in extreme conditions*, CEA/CNRS/AREVA/EDF/French Universities) included in the PACEN Program for their subsequent financial support. This work also benefited from financial support of the French National Research Agency (ANR, project ANR-08-BLAN-0216) and from the CNRS Interdisciplinary Research Program MaPro-Su (*Matériaux et Procédés de Remplacement/Substitution*).

■ REFERENCES

(1) Steele, B. C. H. *Solid State Ionics* **2000**, *129*, 95–110.
(2) Maki, Y.; Matsuda, M.; Kudo, T. U.S. Patent 3,607,424, 1971.
(3) Omar, S. Ph.D. Thesis, University of Florida, Gainesville, FL, 2008.
(4) Inaba, H.; Tagawa, H. *Solid State Ionics* **1996**, *83*, 1–16.
(5) Stephens, I. E. L.; Kilner, J. A. *Solid State Ionics* **2006**, *177*, 669–676.
(6) Kim, H. S; Joung, C. Y.; Lee, B. H.; Oh, J. Y.; Koo, Y. H.; Heimgartner, P. *J. Nucl. Mater.* **2008**, *378*, 98–104.
(7) Wolcyrz, M.; Kepinski, L. *J. Solid State Chem.* **1992**, *99*, 409–413.
(8) Dedov, N.; Bagryantsev, V. *Radiochemistry* **1996**, *38*, 24–26.
(9) Cooper, M. J. *Acta Crystallogr., Sect. B* **1982**, *38*, 264–269.
(10) Shannon, R. D. *Acta Crystallogr.* **1976**, *A32*, 751–767.
(11) Tommasi, J.; Delpech, M.; Groullier, J.-P.; Zaetta, A. *Nucl. Tech.* **1995**, *111*, 133–148.
(12) http://www.gen-4.org/PDFs/GenIVRoadmap.pdf A technology roadmap for generation IV nuclear energy systems, *Generation IV international forum*, 2002.
(13) CEA/DEN document. *Treatment and recycling of spent nuclear fuel*; Moniteur L., Ed.; Le Moniteur Editions: Paris, 2008, ISBN 978-2-281-11377-8.
(14) Degueldre, C.; Bertsch, J.; Kuri, G.; Martin, M. *Energy Environ. Sci.* **2011**, *4*, 1651–1661.
(15) Haire, R. G.; Eyring, L. R. *Handbook on the Physics and Chemistry on Rare Earths*; Gschneidner, K. A., Eyring, L. R., Choppin, G. R., Landler, G. H., Eds.; North Holland Publishing Company: Amsterdam, 1994; Vol. 3, p 18.
(16) Minervini, L.; Zacate, M. O.; Grimes, R. W. *Solid State Ionics* **1999**, *116*, 339–349.
(17) Guo, X.; Waser, R. *Prog. Mater. Sci.* **2006**, *51*, 151–210.
(18) Ikuma, Y.; Shimada, E.; Okamura, N. *J. Am. Ceram. Soc.* **2005**, *88*, 419–423.
(19) Hong, S. J.; Virkar, A. V. *J. Am. Ceram. Soc.* **1995**, *78*, 433–439.
(20) Chavan, S. V.; Mathews, M. D.; Tyagi, A. K. *Mater. Res. Bull.* **2005**, *40*, 1558–1568.

(21) Hagiwara, T.; Kyo, Z.; Manabe, A.; Yamamura, H.; Nomura, K. *J. Ceram. Soc. Jpn.* **2009**, *117*, 1306–1310.
(22) Nitani, H.; Nakagawa, T.; Yamanouchi, M.; Osuki, T.; Yuya, M.; Yamamoto, T. A. *Mater. Lett.* **2004**, *58*, 2076–2081.
(23) Shuk, P.; Greenblatt, M.; Croft, M. *J. Alloys Compd.* **2000**, *303*, 465–471.
(24) Mandal, B. P.; Grover, V.; Tyagi, A. K. *Mater. Sci. Eng., A* **2006**, *430*, 120–124.
(25) Grover, V.; Tyagi, A. K. *Mater. Res. Bull.* **2004**, *39*, 859–866.
(26) Mandal, B. P.; Roy, M.; Grover, V.; Tyagi, A. K. *J. Appl. Phys.* **2008**, *103*, 033506.
(27) Mandal, B. P.; Grover, V.; Roy, M.; Tyagi, A. K. *J. Am. Ceram. Soc.* **2007**, *90*, 2961–2965.
(28) Malecka, M.; Kepinski, L.; Maczka, M. *J. Solid State Chem.* **2008**, *181*, 2306–2312.
(29) Bevan, D. J. M.; Summerville, E. *Handbook on the Physics and Chemistry on Rare Earths*; Gschneidner, K. A., Eyring, L. R., Eds.; North Holland Publishing Company: New York, 1979; Vol. 3, p 401.
(30) Bellière, V.; Joorst, G.; Stephan, O.; de Groot, F. M. F.; Weckhuysen, B. M. *J. Phys. Chem. B* **2006**, *110*, 9984–9990.
(31) Bae, J. S.; Choo, W. K.; Lee, C. H. *J. Eur. Ceram. Soc.* **2004**, *24*, 1291–1294.
(32) Zinkevich, M. *Prog. Mater. Sci.* **2007**, *52*, 597–647.
(33) Adachi, G.; Imanaka, N. *Chem. Rev.* **1998**, *98*, 1479–1514.
(34) Sibieude, F.; Foex, M. *J. Nucl. Mater.* **1975**, *56*, 229–238.
(35) Warshaw, I.; Roy, R. *J. Phys. Chem.* **1961**, *65*, 2048–2051.
(36) Wilkes, M. F.; Hayden, P.; Bhattacharya, A. K. *J. Catal.* **2003**, *219*, 305–309.
(37) Tianshu, Z.; Hing, P.; Huang, H.; Kilner, J. *Solid State Ionics* **2002**, *148*, 567–573.
(38) Andrievskaya, E. R.; Kornienko, O. A.; Sameljuk, A. V.; Sayir, A. *J. Eur. Ceram. Soc.* **2011**, *31*, 1277–1283.
(39) Van Herle, J.; Horita, T.; Kawada, T.; Sakai, N.; Yokokawa, H.; Doyika, M. *Ceram. Int.* **1998**, *24*, 229–241.
(40) Clavier, N.; Hingant, N.; Rivenet, M.; Obbade, S.; Dacheux, N.; Barré, N.; Abraham, F. *Inorg. Chem.* **2010**, *49*, 1921–1931.
(41) Arab-Chapelet, B.; Grandjean, S.; Nowogrocki, G.; Abraham, F. *J. Nucl. Mater.* **2008**, *373*, 259–268.
(42) B. Arab-Chapelet, B.; Grandjean, S.; Nowogrocki, G.; Abraham, F. *J. Alloy. Compd.* **2007**, *444*, 387–390.
(43) Hingant, N.; Clavier, N.; Dacheux, N.; Hubert, S.; Barré, N.; Podor, R.; Aranda, L. *Powder Technol.* **2011**, *208*, 454–460.
(44) Hingant, N.; Clavier, N.; Dacheux, N.; Barré, N.; Hubert, S.; Obbade, S.; Taborda, F.; Abraham, F. *J. Nucl. Mater.* **2009**, *385*, 400–406.
(45) Heisbourg, G.; Hubert, S.; Dacheux, N.; Ritt, J. *J. Nucl. Mater.* **2003**, *321*, 141–151.
(46) Hubert, S.; Heisbourg, G.; Dacheux, N.; Moisy, P. *Inorg. Chem.* **2008**, *47*, 2064–2073.
(47) Heisbourg, G.; Hubert, S.; Dacheux, N.; Purans, J. *J. Nucl. Mater.* **2004**, *335*, 5–13.
(48) Hubert, S.; Barthelet, K.; Fourest, B.; Lagarde, G.; Dacheux, N.; Baglan, N. *J. Nucl. Mater.* **2001**, *297*, 206–213.
(49) Morris, D. E.; Hobart, D. E. *J. Raman Spectrosc.* **1988**, *19*, 231–237.
(50) Ubaldini, A.; Artini, C.; Costa, G. A.; Carnasciali, M. M.; Masini, R. *J. Therm. Anal. Calorim.* **2008**, *91*, 797–803.
(51) Ollendorff, W.; Weigel, F. *Inorg. Nucl. Chem. Lett.* **1969**, *5*, 263–269.
(52) Krishnamurty, K. V.; Harris, G. M. *Chem. Rev.* **1960**, *61*, 213–246.
(53) Vickery, R. C. *Chemistry of the Lanthanon*;Butterworths Scientific Publications: London, 1953.
(54) Rodriguez-Carvajal, J. *Physica B* **1993**, *192*, 55–69.
(55) Hussein, G. A. M.; Khedr, M. H.; Farghali, A. A. *Colloids Surf. A* **2002**, *203*, 137–142.
(56) Balboul, B. A. A. *Thermochim. Acta* **2000**, *351*, 55–60.
(57) Cullity, B. D.; Stock, S. R., *Elements of X-Ray Diffraction*, 3rd ed.; Prentice-Hall Inc.: New York, 2001.
(58) Ou, D. R.; Mori, T.; Ye, F.; Zou, J.; Auchterlonie, G.; Drennan, J. *Phys. Rev. B* **2008**, *77*, 024108.
(59) Levy, M. R.; Stanek, C. R.; Chroneos, A.; Grimes, R. W. *Solid State Science* **2007**, *9*, 588–593.
(60) Dachs, H. *Z. Kristallogr.* **1956**, *107*, 370–395.
(61) Larroque, P. *L'observation des domaines antiphases dans les alliages.* Annales de la faculté des sciences de Toulouse, **1961**, *25*, 209.
(62) Ye, F.; Mori, T.; Ou, D. R.; Zou, J.; Drennan, J. *Mater. Res. Bull.* **2008**, *43*, 759–764.
(63) Grover, V.; Banerji, A.; Sengupta, P.; Tyagi, A. K. *J. Solid State Chem.* **2008**, *181*, 1930–1935.
(64) McBride, J. R.; Hass, K. C.; Poindexter, B. D.; Weber, W. H. *J. Appl. Phys.* **1994**, *76*, 2435–2441.
(65) Weber, W. H.; Hass, K. C.; McBride, J. R. *Phys. Rev. B* **1993**, *48*, 178–185.
(66) Ohashi, T.; Yamazaki, S.; Tokunagaa, T.; Arita, Y.; Matsui, T.; Harami, T.; Kobayashi, K. *Solid State Ionics* **1998**, *113−115*, 559–564.
(67) Yamazaki, S.; Matsui, T.; Ohashi, T.; Arita, Y. *Solid State Ionics* **2000**, *136*, 913–920.
(68) Nakajima, A.; Yoshihara, A.; Ishigame, M. *Phys. Rev. B* **1994**, *50*, 13297–13307.
(69) Dohčević-Mitrović, Z. D.; Radović, M.; Šćepanović, M.; Grujić-Brojčin, M.; Popović, Z. V.; Matović, B.; Bošković, S. *Appl. Phys. Lett.* **2007**, *91*, 203118.
(70) Denning, J. H.; Ross, S. D. *J. Phys. C: Solid State Phys.* **1972**, *5*, 1123–1133.
(71) Wagemaker, M.; Borghols, W. J. H; Mulder, F. M. *J. Am. Chem. Soc.* **2007**, *129*, 4323–4327.
(72) Meethong, N.; Huang, H.-Y. S.; Carter, W. C.; Chiang, Y.-M. *Electrochem. Solid St. Lett.* **2007**, *10*, A134–A138.
(73) Wagemaker, M.; Mulder, F. M.; Van der Ven, A. *Adv. Mater.* **2009**, *21*, 2703–2709.
(74) Chavan, S. V.; Tyagi, A. K. *Mater. Sci. Eng., A* **2005**, *404*, 57–63.
(75) Bevan, D. J. M.; Barker, W. W.; Martin, R. L. *Proceedings of the Fourth Conference on Rare Earths Research*; Gordon and Breach: New York, 1964, 441.
(76) Hayashi, H.; Sagawa, R.; Inaba, H.; Kawamura, K. *Solid State Ionics* **2000**, *131*, 281–290.
(77) Vegard, L. *Z. Phys.* **1921**, *5*, 17–26.
(78) Denton, A. R.; Ashcroft, N. W. *Phys. Rew. A* **1991**, *43*, 3161–3164.
(79) Jensen, L. L.; Muckerman, J. T.; Newton, M. D. *J. Phys. Chem. C* **2008**, *112*, 3439–3446.
(80) Li, Y.-F.; Ouyang, J.-H.; Zhou, Y.; Liang, X.-S.; Zhong, J.-Y. *Bull. Mater. Sci.* **2009**, *32*, 149–153.
(81) Bommer, H. *Z. Anorg. Allg. Chem.* **1939**, *241*, 273–280.
(82) Aizenshtein, M.; Shvareva, T. Y.; Navrotsky, A. *J. Am. Ceram. Soc.* **2010**, *93*, 4142–4147.
(83) Zimmer, E.; Merz, E. *J. Nucl. Mater.* **1984**, *124*, 64–67.
(84) Uriarte, A.; Rainey, R. Dissolution of high-density UO_2, PuO_2 and UO_2-PuO_2 pellets in inorganic acids. U.S. atomic energy commision Report ORNL-3695, Oak-Ridge, TN, 1965.